Journal of Power Sources 255 (2014) 65–69

Contents lists available at ScienceDirect

Journal of Power Sources

journal homepage: www.elsevier.com/locate/jpowsour

Short communication

The inherent kinetic electrochemical reduction of oxygen into H_2O on FeN_4-carbon: A density functional theory study

Jing Zhang [a,b,c], Zhijian Wang [a,*], Zhenping Zhu [a,*]

[a] State Key Laboratory of Coal Conversion, Institute of Coal Chemistry, Chinese Academy of Sciences, Taiyuan, Shanxi 030001, China
[b] School of Chemical and Biological Engineering, Taiyuan University of Science and Technology, Taiyuan, Shanxi 030021, China
[c] University of Chinese Academy of Sciences, Beijing 100039, China

HIGHLIGHTS

- The detailed ORR kinetic mechanism on FeN_4-graphene was studied.
- Both four-electron and two-electron ORR pathways were investigated.
- The ORR favored the four-electron pathway on FeN_4-graphene.
- The rate-determining step of entire pathway was the reduction of O_2 into OOH.

GRAPHICAL ABSTRACT

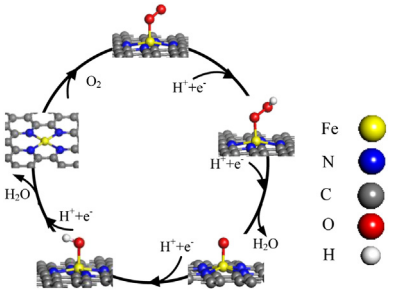

ARTICLE INFO

Article history:
Received 20 October 2013
Received in revised form
17 December 2013
Accepted 2 January 2014
Available online 11 January 2014

Keywords:
Kinetic mechanism
Oxygen reduction reaction (ORR)
Density functional theory (DFT)
Iron-based catalyst
Nitrogen-doped graphene

ABSTRACT

Metal-coordinated nitrogen-doped carbons are highly active in promoting electrochemical oxygen reduction reaction (ORR). This study describes in detail the ORR kinetics on FeN_4-graphene based on a density functional theory calculation. O_2 molecules chemisorbed on Fe site prefer hydrogenation into OOH species rather than direct breakage of the O–O bond. The subsequent reduction of OOH species into H_2O_2 has a slightly high barrier (1.13 eV). However, this barrier could be bypassed by hydrogenation dissociation into O and H_2O, which displays a low barrier (0.47 eV). Further O → OH and OH → H_2O reactions are kinetically simple. Throughout the entire ORR, the initial O_2 → OOH reaction determines the total rate and displays a reaction barrier of 0.62 eV. This kinetic profile suggests that O_2 molecules are inherently favorable for reduction into H_2O on FeN_4-graphene following a four-electron process.

1. Introduction

Oxygen reduction reaction (ORR), which is a cathodic half-reaction, limits the performance of fuel cell in fuel cell system because of its multi-electron reaction character and low reaction rate [1,2]. A high efficient fuel cell requires highly active ORR catalysts to promote the four-electron reduction of O_2 into H_2O [3,4]. Platinum-based catalysts are quite active for ORR, but their problems in durability and cost strongly limit their commercial applications [5,6]. Considerable efforts are focused on developing new affordable and stable catalysts to replace the platinum-based catalysts [6–9], and a variety of non-noble metal catalysts are developed [6]. Among these catalysts, transition metal-coordinated N-doped carbons (MN*x*-C) are proven to be quite catalytically active for ORR compared with normal platinum-based catalysts and exhibit very high stability [10–23]. Given these findings, MN*x*-C are potential materials to substitute platinum-based catalysts. In spite

* Corresponding authors. Tel.: +86 351 4048715; fax: +86 351 4151663.
E-mail addresses: zpzhu@sxicc.ac.cn, mhs913@163.com (Z. Zhu).

0378-7753/$ – see front matter © 2014 Elsevier B.V. All rights reserved.
http://dx.doi.org/10.1016/j.jpowsour.2014.01.008

of significant progress on MN*x*-C catalysts, the nature of the active ORR catalysis of these catalysts remains unclear. Some fundamental challenges, such as active catalytic sites of ORR on MN*x*-C catalysts, are still on debate. Some authors supported that the ORR active sites are the M–N*x*–C*y* moieties [24–27]. Other researchers proposed that transition metal itself does not have a function in the ORR, instead the presence of transition metal center serves to catalyze the formation of N/C catalytically active sites during the pyrolysis procedures [28–30]. He et al. [31] showed that the performance of CuN_x/C is significantly lower than that of FeN_x/C. Their result indicates that the metal has an important function in the electroreduction of oxygen. Bambagioni et al. [32] obtained the same conclusion.

To further optimize the structure and performance of MN*x*-C catalysts, understanding the detailed information in the catalytic reaction thermodynamics and kinetics is necessary. Given that the MN*x*-C catalyst structures are slightly complex, experimental insights into the reaction thermodynamics and kinetics are very difficult. Theoretical calculation is a powerful tool to extract detailed surface reaction information at the molecular level.

Theoretical calculations based on density functional theory (DFT) are applied to MN*x*-C systems for ORR [33–35]. Based on the adsorption behaviors of O_2 and related intermediates on MN*x*-C catalysts, all of the calculations resulted in MN*x*-C systems. Graphitic M–N_4 configuration is energetically favorable and stable in the actual operated potential region [33–35]. Considering the weak interaction between peroxide and CoN_4–C, Kattel et al. [33] proposed that Co–N_4 does not promote entire ORR and a second site for peroxide reduction is required. Calle-Vallejo et al. [34] showed that the adsorption behavior of transition metals is not intrinsic because it can be severely altered by changes in the local geometry of the active site, the chemical nature of the nearest neighbors, and the oxidation states. Kim et al. reported that the Fe sites on FeN_4-carbon nanotubes are stable adsorption sites for O_2 and all intermediate species [35], which is similar to the situation of ORR on metal-N_4 macrocycles [36–41]. Chen et al. [36] combined experimental and theoretical methods to elucidate the mechanisms of ORR on Fe-phthalocyanines (Pc) and CoPc. They suggested that the ORR follows the $4e^-$ route on FePc catalysts, but the $2e^-$ route on CoPc was similar to the results of Sun et al. [37].

The aforementioned studies mainly focused on thermodynamic information, such as the adsorption energies and/or the Gibbs free energy change. However, detailed kinetic behaviors of the MN*x*-C catalysts remain unclear. These behaviors are important to further design and optimize catalyst structure and performance. The present study applied DFT calculations to examine the ORR over the surface of a model FeN_4-graphene (FeN_4-G), which emphasized on the diagnosis of the kinetics of the involved elementary reaction steps.

2. Computational methods and models

2.1. Methods

All calculations were performed within the spin-unrestricted DFT framework as implemented in $DMol^3$ code [42,43]. The Perdew, Burke, and Ernzerhof parameterization of the generalized gradient approximation (GGA) [44] described the electronic exchange and correlation effects [45]. Double numerical plus polarization function basis sets were used in the calculations. A smearing of 0.002 Ha to the orbital occupation was applied to achieve an accurate electronic convergence. A $5 \times 5 \times 1$ *k*-point sampling was used. The geometry convergence tolerance for energy change, max force, and max displacement were 0.00001 hartree, 0.002 hartree/Å, and 0.005 Å, respectively. All atoms were allowed to relax during geometry optimization. The optimized C–C bond length of graphene was 1.42 Å, which agrees well with previous calculations [33]. The adsorption energy E_{ads} is defined as $E_{ads} = E_{tot} - E_{sur} - E_x$, where E_{tot}, E_{sur}, and E_x are the total energies of the FeN_4-G with an adsorbed X species, the FeN_4-G catalysts, and the isolated X species, respectively. A negative adsorption energy indicates that the adsorbate molecule would be energetically favorable to be adducted to the FeN_4-G catalyst. The isolated X species O_2, OOH, OH, O, H_2O_2, and H_2O were optimized in a vacuum box of 15 Å × 15 Å × 15 Å. The optimized O–O bond lengths of O_2 and H_2O_2 were 1.225 and 1.472 Å, respectively, which agree well with previous theoretical O–O bond lengths of 1.22 and 1.48 Å, respectively [33]. The transition states were located through the synchronous method with conjugated gradient refinements. This method involves linear synchronous transit maximization, followed by repeated conjugated gradient (CG) minimizations and quadratic synchronous transit maximizations and repeated CG minimizations until a transition state is located.

2.2. Models

This study used a periodic (6 × 6) supercell of graphene with FeN_4-coordinated structure, which is more favorable energetically than FeN_2 and FeN_3 allotropes [46,47]. Fe, N, and C atoms were all in the same plane in the optimized structure (Fig. 1a). The extracted structural parameters (Table 1) were close to previous calculation results [47], which suggests the reasonability of the present model and calculation condition. The ORR at solid–liquid interfaces was complex because they involved solid surfaces, solvent, and substrates. Therefore, simulating these processes using a simple model system at the solid–gaseous interface seemed difficult. However, the results of these simple models contributed to a better understanding of the complex systems (heterogeneous liquid-phase catalysis).

3. Results and discussion

3.1. Adsorption of O_2 on N-doped FeN_4-G

All possible adsorption sites are considered for O_2 adsorption. The structural optimization shows that the O_2 molecule could only be chemisorbed on Fe with an end-on configuration, which agrees with previous theoretical results [35]. This finding indicates that the Fe site was the active center of the FeN_4-G catalysts [19,24–27]. In addition, the adsorbed O_2 ($O_{2(ads)}$) exhibits two different stable configurations, which incline its head toward the formed five-member ring (Fig. 1b) or six-member ring (Fig. S1). The adsorption energies of the two configurations are −0.95 and −0.80 eV, respectively; the former configuration is considered in the following calculations. After O_2 adsorption, Fe atom protrudes out of the graphene plane (Fig. 1b) with significant extension in Fe–N bonds (Table 1), and the O–O bond extends from 1.225 Å to 1.286 Å. This result indicates a strong interaction between O_2 and iron site and reflects an effective activation of molecular O_2. Table 1 also presents the structural parameters and adsorption energies obtained from the adsorption states related to the entire reaction.

3.2. Chemical behavior of adsorbed oxygen and formation of adsorbed OOH

Under the ORR conditions, the two possible pathways for the surface reaction of $O_{2(ads)}$ are dissociation into $O_{(ads)}$ [Eq. (1)] and hydrogenation into $OOH_{(ads)}$ species [Eq. (2)].

$$O_{2(ads)} \rightarrow 2O_{(ads)} \quad (1)$$

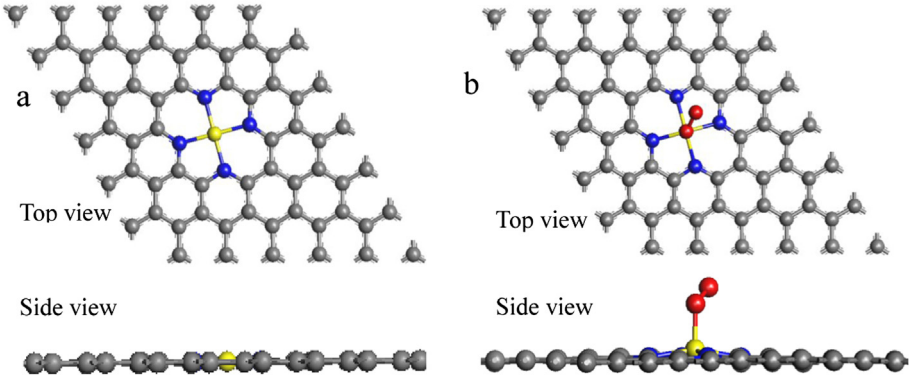

Fig. 1. Top and side views of the most stable configurations of FeN_4-G (a) and O_2 molecule adsorbed FeN_4-G (b). Gray, yellow, red and blue spheres represent C, Fe, O and N atoms, respectively. (For interpretation of the references to color in this figure legend, the reader is referred to the web version of this article.)

$$O_{2(ads)} + H^+ + e^- \rightarrow OOH_{(ads)} \quad (2)$$

$O_{2(ads)}$ dissociation is highly endothermic, with a reaction energy (the change of the total energy between productions and reactants) of 1.02 eV (Fig. S2). The activation barrier of this process is approximately 2.53 eV, which is obviously too high to overcome at the working temperature of fuel cell (approximately 80 °C). In pathway (2), $O_{2(ads)}$ can capture one H^+ and e^- to form $OOH_{(ads)}$. Zhang et al. [48] suggested that O_2 can adsorb H^+ to form H^+OO in acidic environment because the whole system is neutral. OOH^+ could be simplified to OOH, and the subsequent adsorbed H^+ could be taken as H by considering the ionization potentials. Reaction (2) is thermodynamically favorable (Fig. 2) because the OOH species chemisorbed on the iron sites are relatively stable, with an adsorption energy of −1.87 eV. We consider two different situations dependent on the location of H species to investigate the kinetic mechanism of $O_{2(ads)}$ hydrogenation into $OOH_{(ads)}$. When H species are located at the carbon atom (Fig. 2a), capturing of H by $O_{2(ads)}$ is kinetically difficult, with a barrier of 1.60 eV. Alternatively, H species could be stably co-adsorbed at Fe site (Fig. 2b), although it has a total energy slightly higher than the former situation. Kinetically, the O_2 and H species co-adsorbed on Fe site are more favorable for conversion into $OOH_{(ads)}$, with lower reaction barrier (0.62 eV).

3.3. Chemical behavior of adsorbed $OOH_{(ads)}$

The reduction of $OOH_{(ads)}$ into H_2O requires a breakage of the O—O bond either by one-step breakage or H_2O_2-mediated process. The H_2O_2 formation from OOH [Eq. (3)] displays reaction energy and barrier of −1.44 and 1.13 eV, respectively (Fig. 3a). The high barrier indicates that the reduction of $OOH_{(ads)}$ into H_2O is kinetically difficult through the H_2O_2-mediated pathway. This finding is also supported by the fact that the O—O bond length in optimized $H_2O_{2(ads)}$ is 1.960 Å, which is markedly higher than that in free H_2O_2 molecule (1.472 Å). The higher bond length suggests a near breakage, which is similar to the situations on FePc and FeP [36,37]. $H_2O_{2(ads)}$ is unstable and tends to dissociate as $OH_{(ads)}$ because the dissociation process has an extremely low barrier (0.03 eV).

$$OOH_{(ads)} + H^+ + e^- \rightarrow H_2O_{2(ads)} \quad (3)$$

$$OOH_{(ads)} \rightarrow O_{(ads)} + OH_{(ads)} \quad (4)$$

$$OOH_{(ads)} + H^+ + e^- \rightarrow 2OH_{(ads)} \quad (5)$$

$$OOH_{(ads)} + H^+ + e^- \rightarrow H_2O_{(ads)} + O_{(ads)} \quad (6)$$

The one-step breakage of O—O bond in $OOH_{(ads)}$ is possible through the three processes expressed in Eqs. (4)–(6). The direct dissociation of $OOH_{(ads)}$ into $O_{(ads)}$ and $OH_{(ads)}$ [Eq. (4)] exhibits reaction energy and barrier of 0.26 and 1.18 eV, respectively (Fig. S3). It is endothermic and exhibits a high barrier and is thus unfavorable. Alternatively, the O—OH bond may break with the help of H, in which the kinetics highly depends on the position of the introduced H species because of the spatial asymmetry of $OOH_{(ads)}$. When the introduced H species is near the oxygen atom fixed at Fe, the dissociation of $OOH_{(ads)}$ with the help of H species tends to produce $OH_{(ads)}$ following Eq. (5) but exhibits a high reaction barrier (1.14 eV; Fig. 3b). When the introduced H species is near the free oxygen atom in $OOH_{(ads)}$, the H-assisted dissociation of $OOH_{(ads)}$ generates O atom and H_2O [Eq. (6)]. This process is kinetically favorable, with a barrier of 0.47 eV (Fig. 3c). The formed H_2O molecule drifts away from the Fe site because of its low adsorption energy (−0.48 eV), whereas the formed O atom tends to remain adsorbed at the Fe site for further reduction because of its extremely high adsorption energy (−4.37 eV).

The further reduction of $O_{(ads)}$ into H_2O should follow the reactions as shown in Eqs. (7) and (8).

$$O_{(ads)} + H^+ + e^- \rightarrow OH_{(ads)} \quad (7)$$

$$OH_{(ads)} + H^+ + e^- \rightarrow H_2O_{(ads)} \quad (8)$$

These two reactions are also characterized with the H-assisted reduction process, and exhibits reaction energies of −2.24 and −1.87 eV, respectively (Figs. S4 and S5). This finding reveals a highly exothermic feature and thermodynamic favorability. Moreover, their reaction barriers are too small [0.48 eV for reaction (7) and 0.39 eV for reaction (8)], which indicates that they proceed at very high rates.

3.4. Total reaction mechanism

The relative energy and reaction barrier profiles of all reaction steps are presented in Fig. 4, which gives an overall picture of the entire ORR on FeN_4-G. In this figure, the total energy of the O_2-adsorbed FeN_4-G surface is used as the reference energy state. Based on the energy of this state, the relative energies of the states at the subsequent reduction steps are obtained with consideration of the difference in atom composition [48]. The detailed data on the reaction energy and barrier for the different reaction steps are summarized in Table 2. According to the calculated reaction barriers, the reaction pathway (as red line in Fig. 4) is the most favorable pathway throughout the entire ORR. In this pathway, the

Table 1
Summary of structural parameters of the FeN_4-G and related adsorption states. Note: E_{ads}, adsorption energy (eV); h, the elevation of the Fe atoms above the graphene plane h (Å); d, bond length (Å); $d_{N-C}(5)$ and $d_{C-C}(5)$, the corresponding bond length in the five-member ring configuration; $d_{N-C}(6)$ and $d_{C-C}(6)$, the corresponding bond length in the six-member ring configuration.

	FeN_4-G	$O_{2(ads)}$	$OOH_{(ads)}$	$O_{(ads)}$	$OH_{(ads)}$	$H_2O_{2(ads)}$	$H_2O_{(ads)}$
E_{ads}	–	−0.95	−1.87	−4.37	−2.94	−0.64	−0.48
h	0	0.372	0.334	0.430	0.346	0.247	0.187
d_{O-Fe}	–	1.754	1.784	1.654	1.808	1.796	2.029
d_{O-x}	–	1.286	1.468	–	0.985	1.960	0.984
d_{N-Fe}	1.902	1.915	1.917	1.935	1.915	1.919	1.908
$d_{N-C}(5)$	1.380	1.367	1.365	1.366	1.365	1.364	1.368
$d_{N-C}(6)$	1.372	1.372	1.379	1.377	1.377	1.372	1.376
$d_{C-C}(5)$	1.430	1.429	1.429	1.430	1.429	1.432	1.433
$d_{C-C}(6)$	1.440	1.438	1.438	1.438	1.437	1.438	1.441

ORR proceeds through four major steps all characterized as a hydrogenation reduction process. The $O_{2(ads)}$ chemisorbed at active Fe site is initially hydrogenated as $OOH_{(ads)}$, performs a hydrogenation dissociation reaction, and generates $O_{(ads)}$ and $H_2O_{(ads)}$. $O_{(ads)}$ is subsequently hydrogenated as $OH_{(ads)}$ and finally as H_2O. As indicated in Fig. 4, this pathway is thermodynamically feasible and exhibits low reaction barriers. This result indicates that O_2 could be readily reduced on FeN_4-G surface and produce H_2O following the four-electron reaction. The highest barrier (0.62 eV) appears at the initial reduction step of the $O_{2(ads)}$-to-$OOH_{(ads)}$ reaction, which acts as the rate-determining step. The relatively low value of the barrier in this rate-determining step reflects that the ORR could intrinsically proceeds at a high rate, which agrees with the experimental observations [10,21]. This event differs from the situation of metal-free N-doped carbons, where the removal of $O_{(ads)}$ reaction is the rate-determining step [49]. This phenomenon indicates that the O_2 reduction could end at the two-electron reduction stage for H_2O_2 formation. Combined with the high barrier in $OOH_{(ads)}$-to-$H_2O_{2(ads)}$ and the instability of the H_2O_2 adsorbed on FeN_4-G, the optimized kinetic profile on FeN_4-G suggests that the four-electron reduction of O_2 into H_2O is inherently favorable.

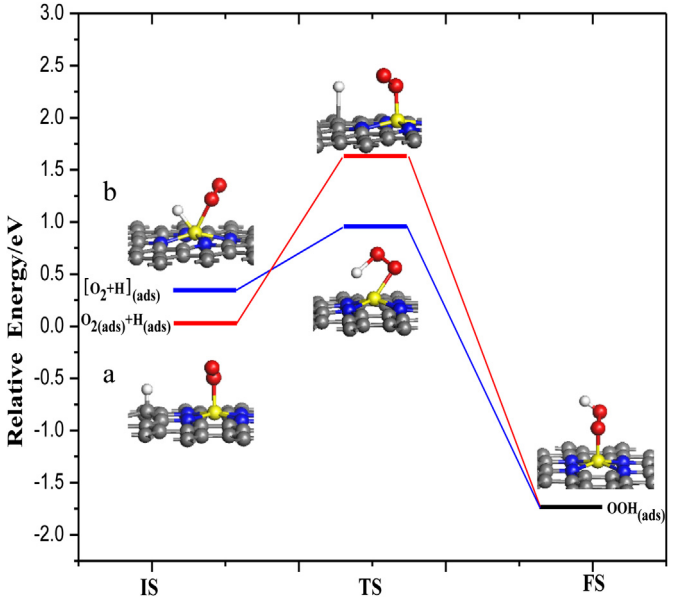

Fig. 2. Optimized structures for the initial states (IS), transition states (TS), and final states (FS) of O_2 reduction into OOH on FeN_4-G together with corresponding activation barrier and relative reaction energy. (a) O_2 and H species adsorbed on different sites of FeN_4-G. (b) Both O_2 and H species are chemisorbed on the Fe site.

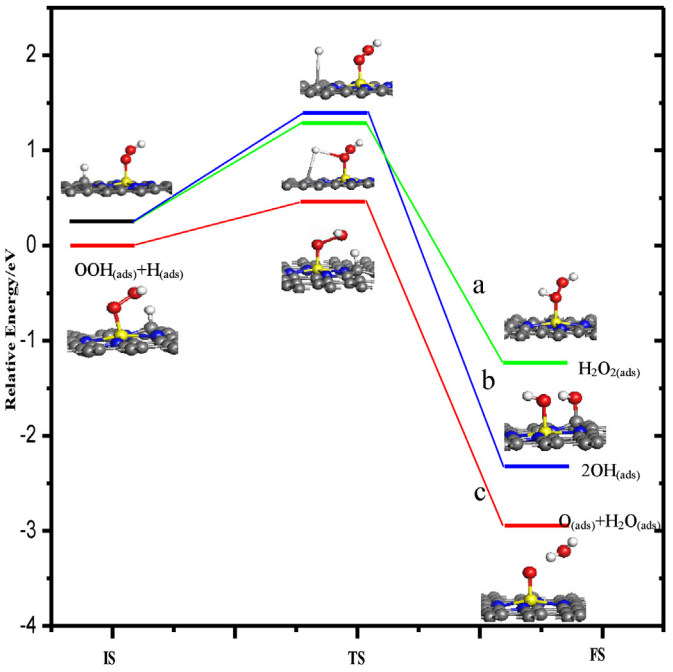

Fig. 3. Optimized structures for the initial states (IS), transition states (TS), and final states (FS) of OOH reduction on FeN_4-G together with corresponding activation barrier and relative reaction energy. (a) OOH reduction into $H_2O_{2(ads)}$, (b) OOH reduction into $OH_{(ads)}$, (c) OOH reduction into $O_{(ads)}$ and $H_2O_{(ads)}$.

Electrochemical reactions on catalysts are too complex to be simulated by a complete theoretical description. The reaction mechanism may quantitatively depend on a number of factors, such as electrode potential, electrolyte, and adsorbate coverage. Thus, the main features of the ORR mechanism may be qualitatively provided by this simulation. The combination of experimental electrochemical measurements (transmission electron microscopy,

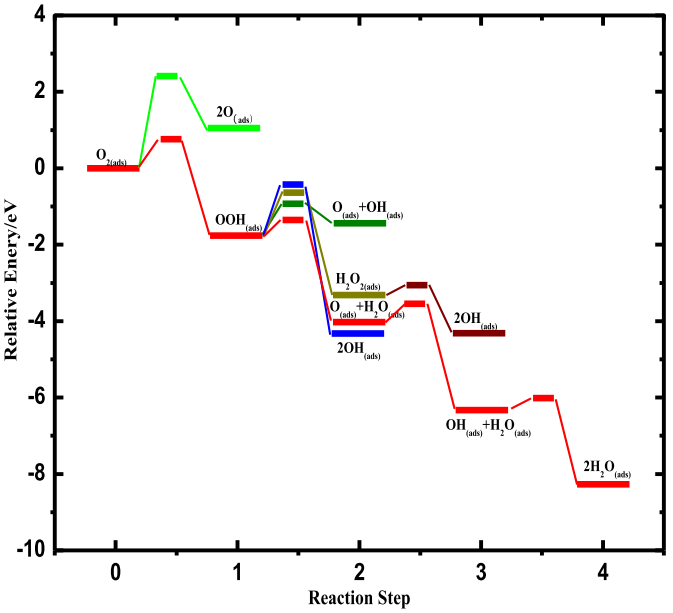

Fig. 4. Calculated relative energies and activation barriers of full reaction pathways for the ORR on FeN_4-G. The initial or final states and transition states are expressed as long and short lines, respectively. The most favorable reaction pathway is expressed as red lines. (For interpretation of the references to color in this figure legend, the reader is referred to the web version of this article.)

Table 2
The reaction energies (ΔE) and activation barriers (E_{act}) of different elemental reaction steps.

Reaction step	ΔE (eV)	E_{act} (eV)
$O_{2(ads)} \rightarrow 2O_{(ads)}$	1.02	2.53
$O_{2(ads)} + H_{(ads)} \rightarrow OOH_{(ads)}$	−2.09	0.62
$OOH_{(ads)} \rightarrow O_{(ads)} + OH_{(ads)}$	0.26	1.18
$OOH_{(ads)} + H_{(ads)} \rightarrow O_{(ads)} + H_2O_{(ads)}$	−2.96	0.47
$OOH_{(ads)} + H_{(ads)} \rightarrow 2OH_{(ads)}$	−2.60	1.14
$OOH_{(ads)} + H_{(ads)} \rightarrow H_2O_{2(ads)}$	−1.44	1.13
$H_2O_{2(ads)} \rightarrow 2OH_{(ads)}$	−1.16	0.03
$O_{(ads)} + H_{(ads)} \rightarrow OH_{(ads)}$	−2.24	0.48
$OH_{(ads)} + H_{(ads)} \rightarrow H_2O_{(ads)}$	−1.87	0.39

rotating ring-disk electrode, and so on) and theoretical modeling is an efficient approach to the investigation of ORR mechanisms and identification of high-performance catalysts for ORR. Therefore, more evidence is needed to support our conclusions in this simulation for future experiments.

4. Conclusions

A DFT calculation is performed on the detailed kinetic and thermodynamic behavior of the ORR on FeN_4-G. Metal-free N-doped carbons are active for ORR [4,8,9], but the O_2 molecule is always chemisorbed at Fe site for the FeN_4-G catalysts. The adsorbed O_2 is then gradually reduced into H_2O through the four hydrogenation-related processes: $O_{2(ads)} \rightarrow OOH_{(ads)} \rightarrow O_{(ads)} + H_2O_{(ads)} \rightarrow OH_{(ads)} + H_2O_{(ads)} \rightarrow 2H_2O_{(ads)}$. The rate-determining step appears at the initial reduction step, $O_{2(ads)}$-to-$OOH_{(ads)}$ reaction. This finding suggests that the ORR efficiency over the catalysts is similar to FeN_4-G, which could be increased by improving O_2 adsorption and activation. Throughout the entire ORR process on FeN_4-G, the two-electron pathway toward H_2O_2 is unfavorable. The four-electron reduction of O_2 into H_2O could readily proceed by a more comfortable kinetic profile, bypassing H_2O_2 formation. This finding shows the unique catalytic nature of FeN_4-G in the ORR process. Further investigations on the ORR kinetic behavior of MN*x*-C catalysts with different metals, N-configurations, and carbon structures is interesting for the design and improvement of catalyst structure and ORR efficiency.

Acknowledgment

The calculations were performed at the Shanghai Supercomputing Center. This work was supported by the Natural Science Foundation of China (nos. 20673135 and 50702065), Shanxi Natural Science Foundation (2012011020-1), and Knowledge Innovation Project of Chinese Academy of Science (no. KJCX2.YW.M10).

Appendix A. Supplementary data

Supplementary data related to this article can be found at http://dx.doi.org/10.1016/j.jpowsour.2014.01.008.

References

[1] B.C.H. Steele, A. Heinzel, Nature 414 (2001) 345–352.
[2] R. Borup, J. Meyers, B. Pivovar, Y.S. Kim, R. Mukundan, N. Garland, D. Myers, M. Wilson, F. Garzon, D. Wood, Chem. Rev. 107 (2007) 3904–3951.
[3] M. Winter, R.J. Brodd, Chem. Rev. 104 (2004) 4245–4270.
[4] L. Qu, Y. Liu, J.B. Baek, L. Dai, ACS Nano 4 (2010) 1321–1326.
[5] J. Greeley, I.E.L. Stephens, A.S. Bondarenko, T.P. Johansson, H.A. Hansen, T.F. Jaramillo, J. Rossmeisl, I. Chorkendorff, J.K. Nørskov, Nat. Chem. 1 (2009) 552–556.
[6] A. Morozan, B. Jousselme, S. Palacin, Energy Environ. Sci. 4 (2011) 1238–1254.
[7] C.W.B. Bezerra, L. Zhang, K. Lee, H. Liu, A.L.B. Marques, E.P. Marques, H. Wang, J. Zhang, Electrochim. Acta 53 (2008) 4937–4951.
[8] K. Gong, F. Du, Z. Xia, M. Durstock, L. Dai, Science 323 (2009) 760–764.
[9] R. Liu, D. Wu, X. Feng, K. Müllen, Angew. Chem. Int. Ed. 122 (2010) 2619–2623.
[10] M. Lefèvre, E. Proietti, F. Jaouen, J.P. Dodelet, Science 324 (2009) 71–74.
[11] A.B. Anderson, R.A. Sidik, J. Phys. Chem. B 108 (2004) 5031–5035.
[12] S.T. Chang, C.H. Wang, H.Y. Du, H.C. Hsu, C.M. Kang, C.C. Chen, J.C.S. Wu, S.C. Yen, W.F. Huang, L.C. Chen, Energy Environ. Sci. 5 5305–5314.
[13] E.B. Easton, A. Bonakdarpour, J. Dahn, Electrochem. Solid-State Lett. 9 (2006) A463–A467.
[14] J. Fournier, G. Lalande, R. Côté, D. Guay, J.P. Dodelet, J. Electrochem. Soc. 144 (1997) 218–226.
[15] Y. Kiros, Int. J. Electrochem. Sci. 2 (2007) 285–300.
[16] U.I. Koslowski, I. Abs-Wurmbach, S. Fiechter, P. Bogdanoff, J. Phys. Chem. C 112 (2008) 15356–15366.
[17] S. Pylypenko, S. Mukherjee, T.S. Olson, P. Atanassov, Electrochim. Acta 53 (2008) 7875–7883.
[18] T. Schilling, M. Bron, Electrochim. Acta 53 (2008) 5379–5385.
[19] M.S. Thorum, J.M. Hankett, A.A. Gewirth, J. Phys. Chem. Lett. 2 (2011) 295–298.
[20] A. Velazquez-Palenzuela, L. Zhang, L. Wang, P.L. Cabot, E. Brillas, K. Tsay, J. Zhang, Electrochim. Acta 56 (2011) 4744–4752.
[21] G. Wu, K.L. More, C.M. Johnston, P. Zelenay, Science 332 (2011) 443–447.
[22] D. Yu, Y. Xue, L. Dai, J. Phys. Chem. Lett. 3 (2012) 2863–2870.
[23] M. Yuasa, A. Yamaguchi, H. Itsuki, K. Tanaka, M. Yamamoto, K. Oyaizu, Chem. Mater. 17 (2005) 4278–4281.
[24] A. Bouwkamp-Wijnoltz, W. Visscher, J. Van Veen, E. Boellaard, A. Van der Kraan, S. Tang, J. Phys. Chem. B 106 (2002) 12993–13001.
[25] J. Maruyama, C. Baier, H. Wolfschmidt, P. Bele, U. Stimming, Electrochim. Acta 63 (2012) 16–21.
[26] J. Maruyama, N. Fukui, M. Kawaguchi, I. Abe, J. Power Sources 182 (2008) 489–495.
[27] C. Medard, M. Lefevre, J. Dodelet, F. Jaouen, G. Lindbergh, Electrochim. Acta 51 (2006) 3202–3213.
[28] S. Maldonado, K.J. Stevenson, J. Phys. Chem. B 108 (2004) 11375–11383.
[29] S. Maldonado, K.J. Stevenson, J. Phys. Chem. B 109 (2005) 4707–4716.
[30] H. Paul, E. Wang, J.M.M. Millet, U.S. Ozkan, J. Phys. Chem. C 111 (2007) 1444–1450.
[31] Q. He, X. Yang, R. He, A. Bueno-López, H. Miller, X. Ren, W. Yang, B.E. Koel, J. Power Sources 213 (2012) 169–179.
[32] V. Bambagioni, C. Bianchini, J. Filippi, A. Lavacchi, W. Oberhauser, A. Marchionni, S. Moneti, F. Vizza, R. Psaro, V. Dal Santo, A. Gallo, S. Recchia, L. Sordelli, J. Power Sources 196 (2011) 2519–2529.
[33] S. Kattel, P. Atanassov, B. Kiefer, Phys. Chem. Chem. Phys. 15 (2013) 148–153.
[34] F. Calle-Vallejo, J.I. Martínez, J. Rossmeisl, Phys. Chem. Chem. Phys. 13 (2011) 15639–15643.
[35] D.H. Lee, W.J. Lee, W.J. Lee, S.O. Kim, Y.-H. Kim, Phys. Rev. Lett. 106 (2011) 175502–175504.
[36] R. Chen, H. Li, D. Chu, G. Wang, J. Phys. Chem. C 113 (2009) 20689–20697.
[37] S. Sun, N. Jiang, D. Xia, J. Phys. Chem. C 115 (2011) 9511–9517.
[38] G. Wang, N. Ramesh, A. Hsu, D. Chu, R. Chen, Mol. Simul. 34 (2008) 1051–1056.
[39] X. Chen, F. Li, X. Wang, S. Sun, D. Xia, J. Phys. Chem. C 116 (2012) 12553–12558.
[40] X. Chen, S. Sun, X. Wang, F. Li, D. Xia, J. Phys. Chem. C 116 (2012) 22737–22742.
[41] Z. Shi, H. Liu, K. Lee, E. Dy, J. Chlistunoff, M. Blair, P. Zelenay, J. Zhang, Z.S. Liu, J. Phys. Chem. C 115 (2011) 16672–16680.
[42] B. Delley, J. Chem. Phys. 92 (1990) 508–518.
[43] B. Delley, J. Chem. Phys. 113 (2000) 7756–7765.
[44] J.P. Perdew, J. Chevary, S. Vosko, K.A. Jackson, M.R. Pederson, D. Singh, C. Fiolhais, Phys. Rev. B 46 (1992) 6671–6687.
[45] J.P. Perdew, K. Burke, M. Ernzerhof, Phys. Rev. Lett. 77 (1996) 3865–3868.
[46] S. Kattel, P. Atanassov, B. Kiefer, J. Phys. Chem. C 116 (2012) 8161–8166.
[47] A. Titov, P. Zapol, P. Král, D.J. Liu, H. Iddir, K. Baishya, L.A. Curtiss, J. Phys. Chem. C 113 (2009) 21629–21634.
[48] L. Zhang, Z. Xia, J. Phys. Chem. C 115 (2011) 11170–11176.
[49] L. Yu, X. Pan, X. Cao, P. Hu, X. Bao, J. Catal. 282 (2011) 183–190.